Article

Sea Urchin-like Si@MnO₂@rGO as Anodes for High-Performance Lithium-Ion Batteries

Jiajun Liu, Meng Wang, Qi Wang, Xishan Zhao, Yutong Song, Tianming Zhao [ID] **and Jing Sun** *

College of Sciences, Northeastern University, Shenyang 110819, China; 2000165@stu.neu.edu.cn (J.L.); 2000176@stu.neu.edu.cn (M.W.); wangqi@mail.neu.edu.cn (Q.W.); 2000189@stu.neu.edu.cn (X.Z.); 2000172@stu.neu.edu.cn (Y.S.); zhaotm@stumail.neu.edu.cn (T.Z.)
* Correspondence: sunjing74@mail.neu.edu.cn; Tel.: +86-136-0407-3045

Abstract: Si is a promising material for applications as a high-capacity anode material of lithium-ion batteries. However, volume expansion, poor electrical conductivity, and a short cycle life during the charging/discharging process limit the commercial use. In this paper, new ternary composites of sea urchin-like Si@MnO₂@reduced graphene oxide (rGO) prepared by a simple, low-cost chemical method are presented. These can effectively reduce the volume change of Si, extend the cycle life, and increase the lithium-ion battery capacity due to the dual protection of MnO₂ and rGO. The sea urchin-like Si@MnO₂@rGO anode shows a discharge specific capacity of 1282.72 mAh g^{-1} under a test current of 1 A g^{-1} after 1000 cycles and excellent chemical performance at different current densities. Moreover, the volume expansion of sea urchin-like Si@MnO₂@rGO anode material is ~50% after 150 cycles, which is much less than the volume expansion of Si (300%). This anode material is economical and environmentally friendly and this work made efforts to develop efficient methods to store clean energy and achieve carbon neutrality.

Keywords: Si; MnO₂; rGO; sea urchin-like structure; lithium-ion battery; high performance

1. Introduction

In recent years, environmental pollution caused by carbon emissions has an increasing urgency for developing high-density, long lifetime storage materials or storage devices for clean energy. As a carrier of clean energy, lithium-ion batteries play a pivotal role in the country's goal of achieving carbon neutrality [1–4]. A Silicon-based electrode is one of the most promising candidates as an anode for lithium-ion batteries and is expected to replace the use of a commercial graphite electrode (372 mAh g^{-1}) due to its remarkable theoretical capacity (4200 mAh g^{-1}) [5,6]. It is also widely regarded for its good voltage platform, environmental friendliness, and abundant reserves. Despite these advantages, Si-based lithium-ion batteries still face severe volume expansion during the charging/discharging process, poor electrical conductivity, and a short cycle life [7,8]. The safety hazards and unstable performances of Si materials resist the applications of lithium-ion batteries in commercial use. Therefore, many attempts on modifying Si materials have been made to restrict the volume expansion and enhance electrical conductivity for improving the performance of Si-based lithium-ion batteries [9–12].

The rational design of an anode has been considered as an effective strategy to enhance Si-based lithium-ion batteries' performances [13,14]. Some studies have reported that coating or doping can effectively reduce the large volume changes and the subsequent accumulation of excessive stress during lithiation–delithiation cycles [15–19]. Especially, Si nanospheres are combined with carbon materials, a strategy that aims to provide extra space to accommodate volumes' expansion and improve the electrical conductivity of the electrode, such as Si/ reduced graphene oxide (rGO) and Si/Carbon Nanotube (CNT) [20–22]. However, the size gap between Si nanospheres and rGO sheets is large,

and Si nanospheres tend to agglomerate and do not easily migrate uniformly into the rGO sheets to form a stable structure. It is worth mentioning that transition metal oxides are also good anodes with high theoretical capacity, such as MnO_2 (1233 mAh g^{-1}) [23–28]. In addition, the volume changes of MnO_2 in lithium-ion intercalation and deintercalation is very small. A reasonable coating structure was used to grow MnO_2 evenly outside the Si nanospheres, which can avoid the material crushing and form an unstable solid electrolyte interface (SEI) film due to the volume expansion of Si nanospheres during the circulation process, lowering the capacity. At the same time, rGO has high electrical conductivity and excellent physical properties. The low conductivity of transition metal oxides and Si nanospheres can be compensated by rGO. MnO_2 wraps the Si nanosphere to avoid the agglomeration of the Si nanosphere, increase the contact area with the rGO sheet, ensure the interface strength between MnO_2 and rGO, and improve the structural stability of the material [29–32].

Herein, we propose a simple hydrothermal method to produce sea urchin-like Si@MnO_2@rGO as anodes. In this unique structure, MnO_2 and rGO surrounding Si nanospheres formed a strong armor, relieving the mechanical strain generated by the volume expansion of the Si nanospheres and providing enough space to buffer, which helps provide to a long lifetime. In addition, the sea urchin-like Si@MnO_2@rGO anode showed an initial discharge capacity of 1378.15 mAh g^{-1} at a current density of 0.1 A g^{-1} and a discharge specific capacity was maintained at 1282.72 mAh g^{-1} under a test current of 1 A g^{-1} after more than 1000 cycles, showing excellent chemical performance at different current densities. Therefore, this rational design provides a new route for the development of high-performance Si-based anodes; this work made efforts to store clean energy and achieve carbon neutrality [33,34].

2. Materials and Methods

2.1. Materials

All chemicals were analytical reagent grade and used as received. Graphene oxide (GO) was purchased from XFNANO Materials Tech Co., Ltd, Nanjing, China. Si nanospheres, ethanol, $MnSO_4$, $KMnO_4$, KH550, and $NaBH_4$ were obtained from National Medicines Corporation Ltd, Shanghai, China.

2.2. Preparation of Si@MnO_2@rGO

First, 0.5 g of GO and 0.1 of M $NaBH_4$ were ultrasonically dispersed in 100 mL of deionized water with stirring treatment at 80 °C for 24 h. After cooling to room temperature, the sample was centrifuged to obtain reduced graphene oxide (rGO). The above-prepared rGO of 0.05 g was dispersed in 20 mL of deionized water and sonicated for 30 min, denoted as Solution A.

Then, 0.086 g of Si nanospheres (50 nm) were dispersed in a beaker containing 20 mL of water and 20 mL of alcohol, followed by the addition of 50 μL of KH550 silane coupling reagent. The sample was sonicated for 30 min to form a homogeneous solution, denoted as Solution B. Next, Solution A, Solution B, 0.64 g of $MnSO_4$, and 1 g of $KMnO_4$ were sequentially added in a reaction vessel and stirred with magnetic force for 2 h. The reaction temperatures were set as 20, 50, or 160 °C, respectively. After cooling to room temperature, the products were centrifuged with water and ethanol several times to remove the residual reaction products. A freeze-dried treatment was used to remove the water. Finally, the samples were denoted as Si@MnO_2@rGO-20°C, Si@MnO_2@rGO-50°C, and Si@MnO_2@rGO-160°C, respectively.

The synthesis of Si@MnO_2 was similar to the synthesis Si@MnO_2@rGO, only missing the rGO, denoted as Si@MnO_2-20°C, Si@MnO_2-50°C, and Si@MnO_2-160°C, respectively.

2.3. Electrochemical Measurements

The homogeneous slurry was prepared by mixing Si@MnO_2@rGO, acetylene black, and polyvinylidene fluoride (PVDF) in N-methyl-2-pyrrolidone (NMP) with a mass ratio of

8:1:1. After fully stirring, the prepared slurry was evenly coated on a copper foil by a sputter coater, whose space was 25 μm. The dimeter of electrode was 1.5 cm and the anode material mass load was ~1 mg. The electrolyte of each coin cell was ~45 μL. Then, the electrode sheet was placed into a vacuum drying oven for 12 h at 80 °C. The working electrode was the prepared electrode sheet ($Si@MnO_2@rGO$ composites). The electrolyte was a $LiPF_6$ (1.0 mol L^{-1}) in a 1:1:1 v/v/v mixture of ethylene carbonate, dimethyl carbonate, and ethyl methyl carbonate. The separator was Celgard 2400 (Saibo, Beijing, China). The capacity calculation and cycling rate were set by a battery testing system (CT3008, Kejing, Hefei, China). The galvanostatic charge/discharge (GCD) tests were conducted in the voltage window of 0.1–3.2 V. The cyclic voltammetry curve (CV) was carried out with scan rate of 0.1 mV s^{-1} between the voltage range of 0.1–3.2 V using an electrochemical workstation (CHI 600E, Chenhua, Shanghai, China). The electrochemical impedance spectroscopy (EIS) was performed over the frequency range from 100 kHz to 0.1 Hz with an alternating current (AC) impedance of 5 mV and was also recorded by an electrochemical workstation (CHI 600E, Chenhua, Shanghai, China).

2.4. Materials' Characterization

Field-emission scanning electron microscopy (FE-SEM; SU8010, Hitachi High-Tech, Tokyo, Japan) and field-emission transmission electron microscopy (FE-TEM; JEM2100F, JEOL, Tokyo, Japan) were used to characterize the morphology and elemental distribution of the electrode materials. X-ray diffraction (XRD; Rigaku lnc., Tokyo, Japan) was used to characterize the phases, crystallinity, and crystal structures of the samples. The species and chemical composition of the surface elements of the samples were analyzed using X-ray photoelectron spectroscopy (XPS, Thermo AXIS-SUPRA, Kratos, Manchester, UK).

3. Results and Discussion

3.1. Anode Material Design and Morphology Characterization

Figure 1 shows a schematic of the preparation of the sea urchin-like $Si@MnO_2@rGO$ composites. First, GO sheets were reduced to rGO by a hydrothermal method with $NaBH_4$. Then, the rGO was collected and dispersed in deionized water (Solution A). Next, Si nanospheres were dispersed in a solution of water, alcohol, and the KH550 silane coupling agent (Solution B). The composites were well grafted by KH550, improving the conductivity. Finally, Solution A, Solution B, $KMnO_4$, and $MnSO_4$ were added in a reaction vessel and stirred with magnetic force for 2 h. The reactions were carried out at different temperatures, resulting in different morphologies. Si nanospheres were coated with MnO_2 and rGO, which may have contributed to the KH550. The unique double-layer structure of MnO_2 and rGO effectively mitigated the volume expansion of Si nanospheres during the charging/discharging process. In addition, rGO had excellent electrical conductivity, compensating for the low electrical conductivity of Si nanospheres and MnO_2. This was the basis of the rational design of the Si-based anode material for enhancing lithium-ion battery performance.

Figure 2 shows the morphologies of the materials grown at three different temperatures. The morphology of $Si@MnO_2$-20°C is shown in Figure 2a. The MnO_2 formed disordered and entangled filaments on the surface of Si nanospheres. Figure 2b shows $Si@MnO_2$-20°C at a high magnification. The surface of the material was rough and the diameter of $Si@MnO_2$-20°C particles was 200 nm. Figure 2c is an SEM image of $Si@MnO_2@rGO$-20°C, showing that the rGO covered the $Si@MnO_2$-20°C. However, some MnO_2 nanowires appeared on the surface of rGO, which suggested that the material was not stable. Figure 2d,e show the SEM images of $Si@MnO_2$-50°C at different magnifications, respectively. As shown in Figure 2d, the MnO_2 formed a sea urchin-like shell coating on the surface of Si nanospheres. Figure 2e shows the sea urchin-like $Si@MnO_2$-50°C. The stings (MnO_2) were 100–300 nm in length. Figure 2f shows $Si@MnO_2@rGO$-50°C. The rGO wrapped the $Si@MnO_2$-50°C without obvious damage to the structure. Interestingly, this rGO surface was clean, without any MnO_2 nanowires, indicating the sea urchin-like structure was more

stable. MnO$_2$ nanowires were vertically oriented on the outer layer of the Si nanospheres, imbedding rGO layers, forming a stable structure, which can buffer the excessive expansion of the Si nanospheres during the charging/discharging process and extend the batteries' lifetime. Figure 2g shows the SEM image of Si@MnO$_2$-160°C. The MnO$_2$ nanowires grew longer and coated the surface of the Si nanospheres. Figure 2h is the enlarged view of Figure 2g. The plentiful MnO$_2$ nanowires were interleaved. Figure 2i shows the images of Si@MnO$_2$@rGO-160°C. It can be clearly seen that the MnO$_2$ nanowires were broken and dispersed on the surface of rGO, which indicates that the Si@MnO$_2$@rGO-160°C was not stable enough. The stability of the material is one of the important factors of the lithium-ion batteries' performance. The high stability of the anode material may suggest the long life-time. Therefore, the Si@MnO$_2$@rGO-50°C was chosen for the following test.
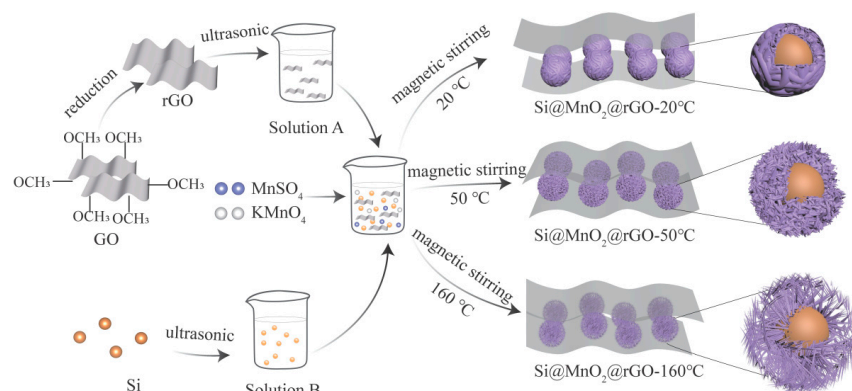

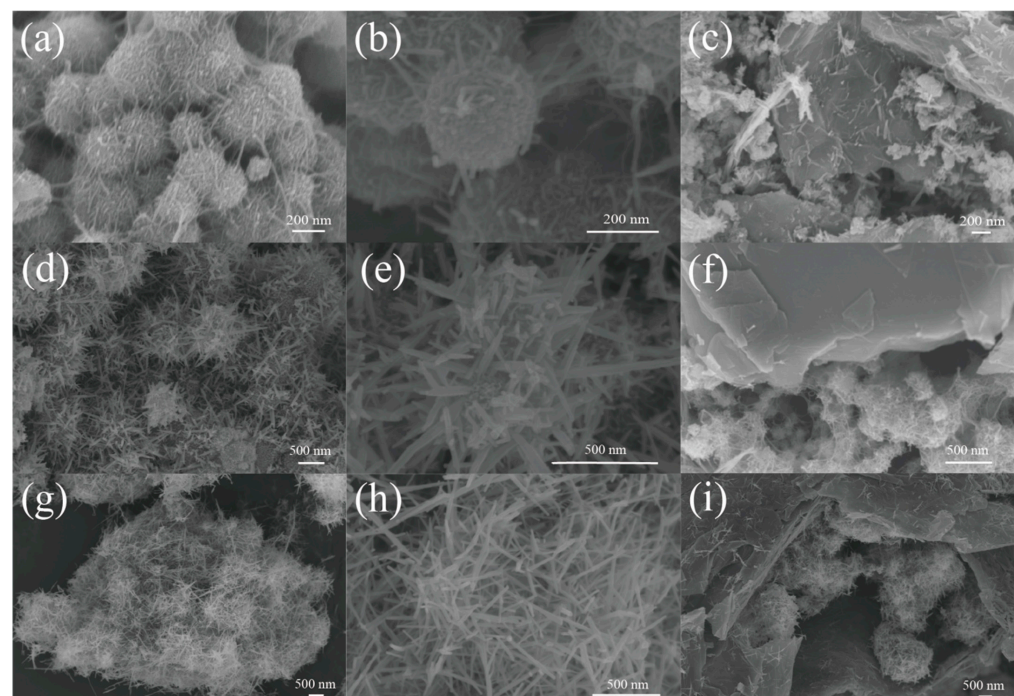**Figure 1.** Concise preparation schematics of the Si@MnO$_2$@ reduced graphene oxide (rGO) composites.

Figure 2. (**a**) SEM image of the Si@MnO$_2$-20°C composite. (**b**) Enlarged view of the SEM image of the Si@MnO$_2$-20°C composite. (**c**) SEM image of the Si@MnO$_2$@rGO-20°C composite. (**d**) SEM image of the Si@MnO$_2$-50°C composite. (**e**) Enlarged view of the SEM image of the Si@MnO$_2$-50°C composite. (**f**) SEM image of the Si@MnO$_2$@rGO-50°C composite. (**g**) SEM image of the Si@MnO$_2$-160°C composite. (**h**) Enlarged view of the SEM image of the Si@MnO$_2$-160°C composite. (**i**) SEM image of the Si@MnO$_2$@rGO-160°C composite.

Figure 3a shows the Energy Dispersive Spectrometer (EDS) analysis of the ball-milled material, using aluminum foil as a substrate, and the inset shows the atomic percentages of elements in the materials. The inset shows that the Si@MnO$_2$@rGO-50°C contained ~48% Si, ~21% rGO, and ~31% MnO$_2$. Table S1 shows the capacity contribution percentages of anode materials (Si, ~63.3%; MnO$_2$, ~35.6%; and rGO, ~1.1%). The existence of MnO$_2$ can not only resist the volume expansion of Si, but also provide the capacity contribution. Figure 3b,c show HRTEM images of the Si@MnO$_2$@rGO-50°C composite at different magnifications. Si nanospheres were coated with rGO and MnO$_2$. The lattice fringes corresponded to the (111) plane of Si, having a separation of 0.31 nm [35,36]. In addition, lattice fringes having an interplanar spacing of 0.47 nm can be seen, and this is consistent with the (200) plane of MnO$_2$ [25,37,38]. The element mapping of the Si@MnO$_2$@rGO-50°C composite is shown in Figure 3d–h. Mn element and O element contributed to MnO$_2$; Si element contributed to Si nanospheres. C element dispersed throughout the image may have contributed to both the substrate and rGO.
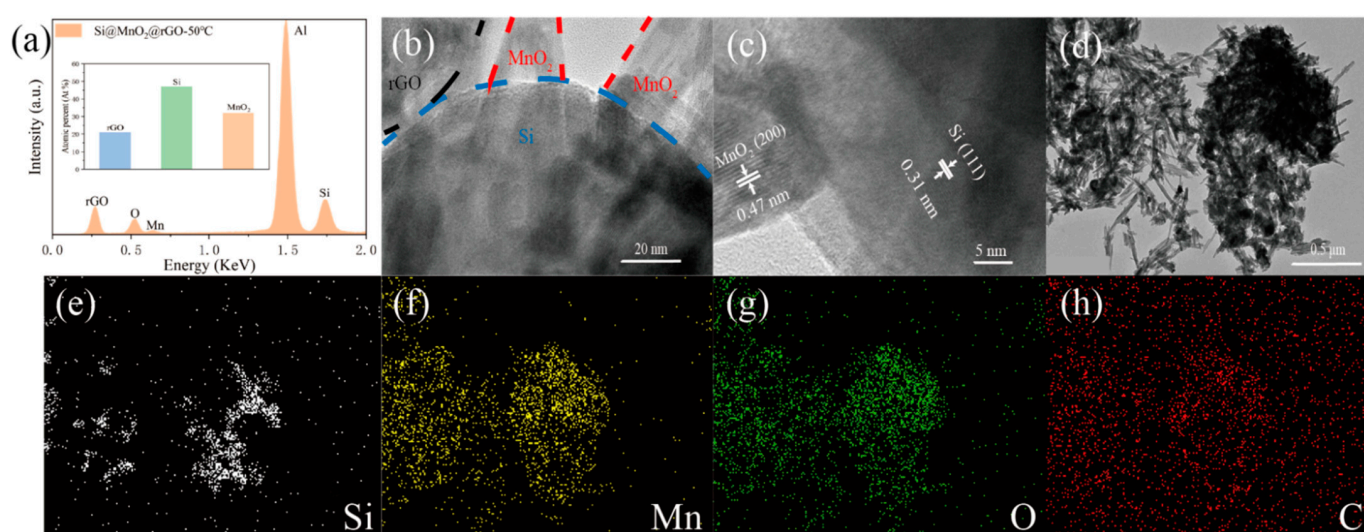

Figure 3. (**a**) Energy Dispersive Spectrometer (EDS) spectra of Si@MnO$_2$@rGO-50°C. Inset showing the respective substance of Si@MnO$_2$@rGO-50°C. (**b**,**c**) HRTEM images of the Si@MnO$_2$@rGO-50°C composite at different magnifications. (**d**–**h**) Elemental mapping of the Si@MnO$_2$@rGO-50°C composite.

Figure 4a shows the XRD patterns of rGO, Si, Si@MnO$_2$-50°C, and Si@MnO$_2$@rGO-50°C, respectively. In the XRD pattern of Si@MnO$_2$-50°C, the pronounced peaks at 28.5°, 47.4°, 56.2°, 58.9°, 69.2°, 76.5°, and 88.2° corresponded to the (111), (220), (311), (222), (400), (331), and (422) planes of Si (PDF#77-2108). In addition, the characteristic peaks at 12.7°, 18.0°, 28.7°, 37.6°, 41.1°, 49.8°, 59.5°, 65.5°, 68.5°, and 72.5° corresponded to the (110), (200), (310), (121), (420), (411), (260), (002), (202), and (631) planes of MnO$_2$ (PDF#72-1982). The XRD pattern of the Si@MnO$_2$@rGO-50°C composites contained peaks corresponding to Si and MnO$_2$, as well as the broad peak ranges from 20° to 30°, which were indexed to the standard peaks of rGO [39–42]. Figure 4b shows the XPS spectrum of the Si@MnO$_2$@rGO-50°C composites, which revealed the presence of Si, Mn, O, and C, corresponding to element mapping (Figure 3d–g). Figure 4c,d shows the high-resolution XPS spectra. Figure 4c shows the Si 2p spectrum, whose peak at 99.7 eV was related to Si-Si bonds; two small peaks at 101.9 and 103.6 eV contributed to organic Si and Si-O, respectively, which may have been caused by the slight oxidation of Si in the thermal-treated process. Figure 4d shows the Mn 2p spectrum, which contained two spin–orbit peaks corresponding to Mn 2p$_{3/2}$ (642.5 eV) and Mn 2p$_{1/2}$ (654.1 eV) of MnO$_2$, whose separation between these peaks was 11.6 eV.
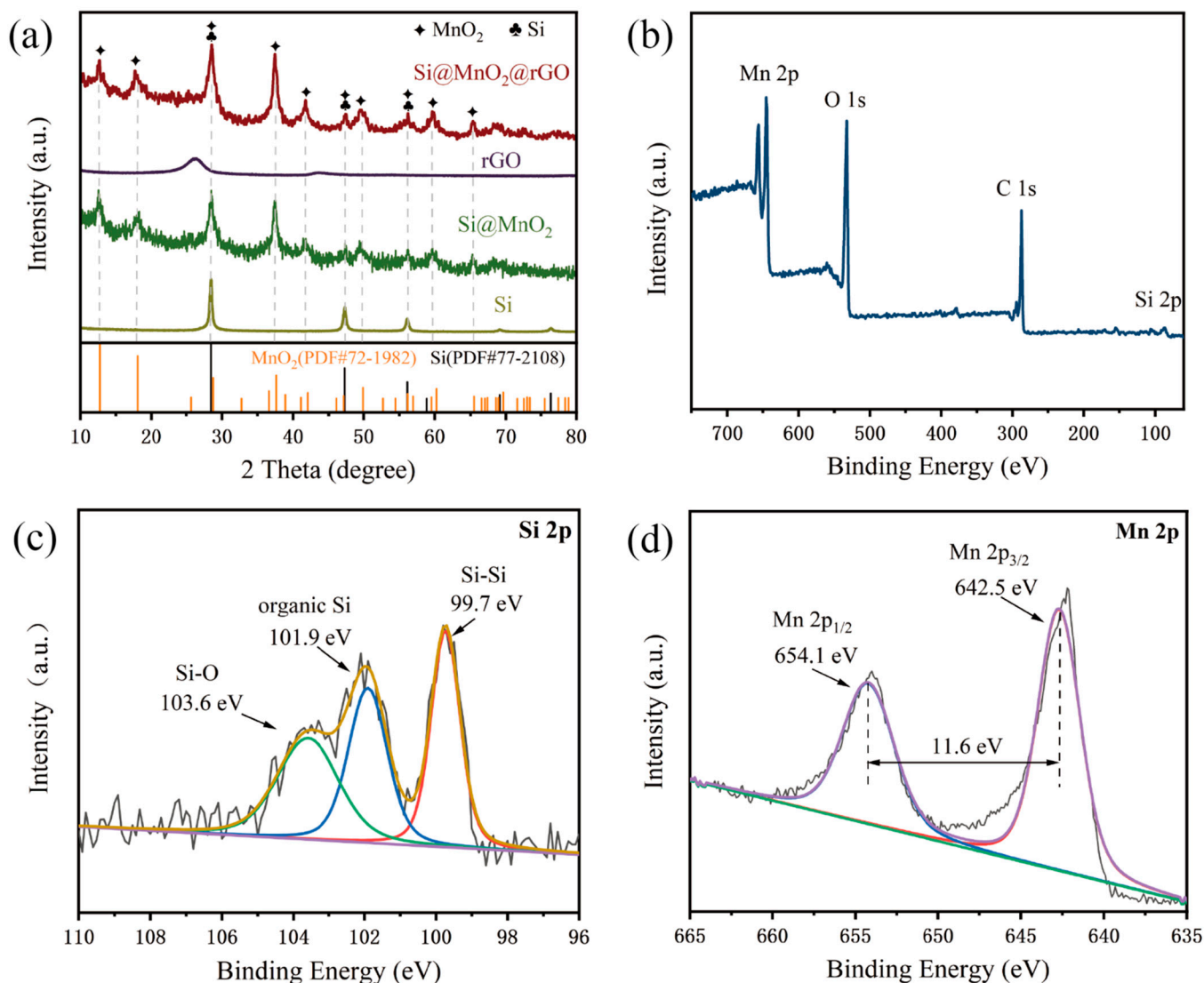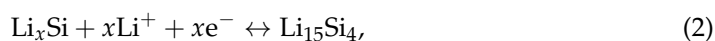
Figure 4. (**a**) X-ray diffraction (XRD) patterns of the Si, Si@MnO$_2$-50°C rGO, and Si@MnO$_2$@rGO-50°C, respectively. (**b**–**d**) XPS spectra of the Si@MnO$_2$@rGO-50°C.

3.2. Lithium-Ion Battery Performance

A CV experiment carried out to further evaluate the lithium storage behavior is shown in Figure 5. Figure 5a shows the CV curves of Si@MnO$_2$@rGO-50°C as the independent anodes of lithium-ion batteries for the first four cycles at a scan rate of 0.1 mV s^{-1} between 0.1 V and 3.2 V. In the first cycle, a clear cathodic peak at 0.16 V corresponded to the lithium alloying process of crystalline Si and the formation of an amorphous Li$_x$Si phase; a clear cathodic peak at 0.10 V corresponded to the formation of the Li$_{15}$Si$_4$ phase. An anodic peak at 0.24 V was related to the delithiation of Li$_{15}$Si$_4$; an anodic peak at 0.50 V was related to the transition from the Li$_x$Si phase to amorphous Si, according to Equations (1) and (2).
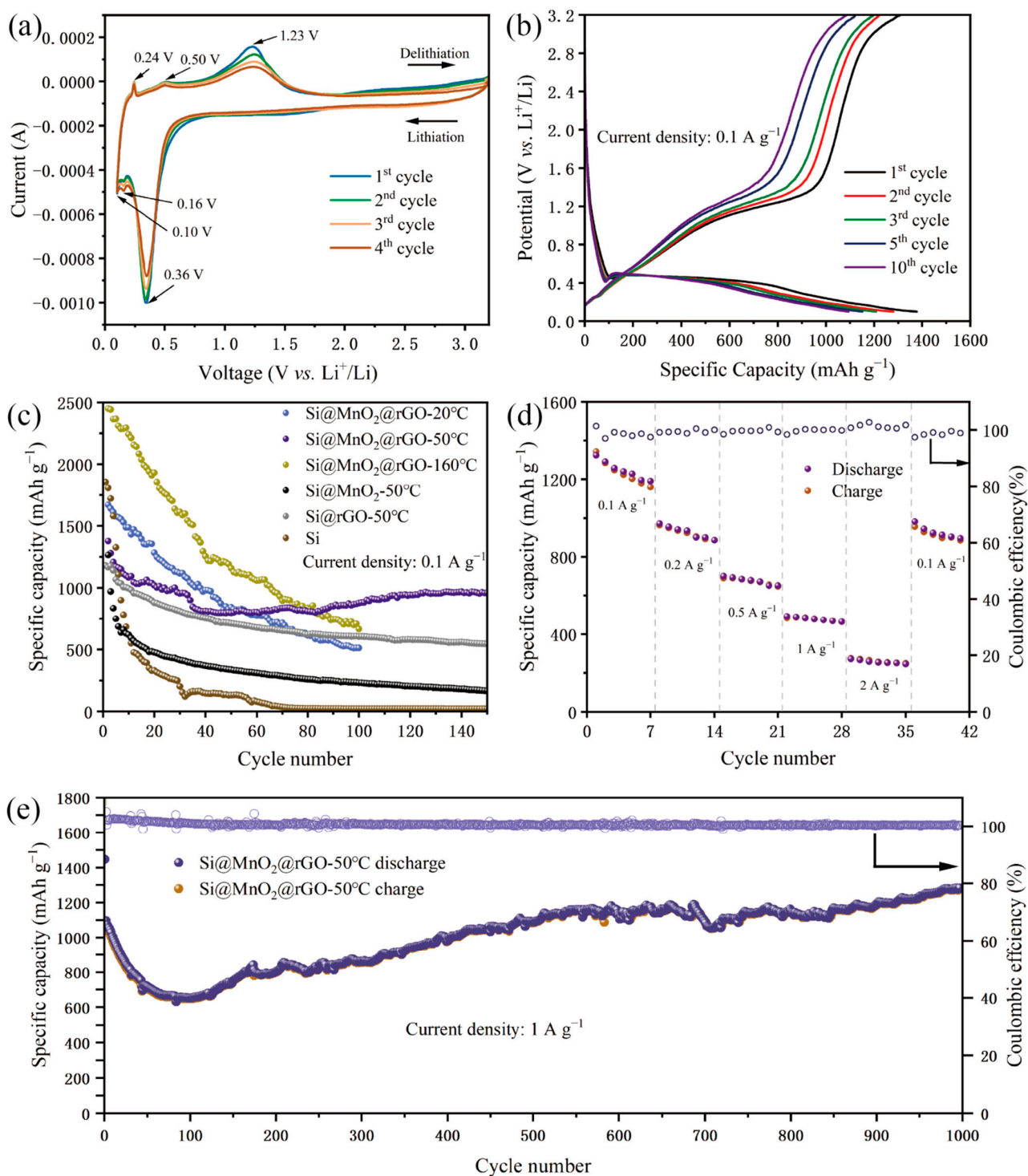
$$x\mathrm{Li}^+ + \mathrm{Si} + x\mathrm{e}^- \leftrightarrow \mathrm{Li}_x\mathrm{Si}, \tag{1}$$

$$\mathrm{Li}_x\mathrm{Si} + x\mathrm{Li}^+ + x\mathrm{e}^- \leftrightarrow \mathrm{Li}_{15}\mathrm{Si}_4, \tag{2}$$

Figure 5. (**a**) CV curves of the Si@MnO$_2$@rGO-50°C at 0.1 mV s^{-1} between 0.1 V and 3.2 V. (**b**) Galvanostatic charge–discharge curves of the Si@MnO$_2$@rGO-50°C at 0.1 A g^{-1}. (**c**) Long-term cycling performance of the Si, Si@MnO$_2$-50°C, Si@rGO-50°C, Si@MnO$_2$@rGO-20°C, Si@MnO$_2$@rGO-50°C, and Si@MnO$_2$@rGO-160°C at 0.1 A g^{-1}. (**d**) Rate performance of the Si@MnO$_2$@rGO-50°C. (**e**) Long-term cycling performance of the Si@MnO$_2$@rGO-50°C at 1 A g^{-1}.

The redox peaks of Si coincided with those reported previously [43–45]. In addition, the reversible redox peaks at 1.23 and 0.36 V, respectively, were consistent with the lithiation and delithiation reactions of MnO$_2$, according to Equation (3). When the cathodic peak was 0.36 V, Li was inserted into the anode to form LiO$_2$ and MnO$_2$ was reduced to Mn. An

anodic peak at 1.23 V was related to the charging process of the lithium ion battery; Mn can facilitate the decomposition of LiO_2.

$$MnO_2 + 4\,Li \leftrightarrow 2\,Li_2O + Mn, \tag{3}$$
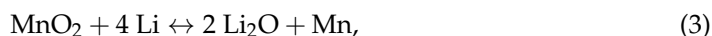
In the subsequent scans, the redox peaks were largely coincident, which was attributed to the stability of the Si@MnO$_2$@rGO-50°C, indicating the good electrochemical reversibility for lithium-ion batteries.

Figure 5b shows the galvanostatic discharge/charge curves of Si@MnO$_2$@rGO-50°C at 0.1 A g^{-1} over the range between 0.1 V and 3.2 V. In the first cycle, the initial discharge capacity was 1378.15 mAh g^{-1}. In the second, third, fifth, and 10th cycles, the discharge specific capacities were 1279.21, 1208.02, 1150.74, and 1093.70 mAh g^{-1}, respectively. In the subsequent cycles, the charge and discharge curves basically overlapped, which indicated good capacity retention. In addition, the plateau of Si at 0.5 V in the figure was consistent with the CV results.

Figure 5c shows the cycling performances of the anode (Si, Si@MnO$_2$-50°C, Si@MnO$_2$@rGO-20°C, Si@MnO$_2$@rGO-50°C, and Si@MnO$_2$@rGO-160°C) at a current density of 0.1 A g^{-1}. Of these samples, Si@MnO$_2$@rGO-50°C showed the best cycling performance. The initial discharge specific capacity of Si was 1855.62 mAh g^{-1}. However, after 20 cycles, the discharge specific capacity decayed to 330.03 mAh g^{-1}; after 150 cycles, the discharge specific capacity was almost 0. This is because, during the cycling process, the slurry of the active material became dislodged from the collector due to the serious volume expansion of Si nanospheres caused by lithium-ion intercalation and deintercalation. When the Si nanospheres underwent volume changes during the charging/discharging process, the formed SEI film was broken, resulting in new surfaces being exposed in the electrolyte. The exposed surfaces needed external lithium ions to form a stable SEI film, which led to a dramatic decrease in capacity. Although Si@MnO$_2$-50°C had a higher discharge specific capacity than Si nanospheres alone after 150 cycles, it still did not meet current demands for battery energy storage. The initial specific capacity of Si@rGO-50°C was 1180.41 mAh g^{-1}; after 150 cycles, the capacity was maintained at 543.84 mAh g^{-1} (Figure 5c). Compared with Si@rGO-50°C and Si@MnO$_2$@ rGO-50°C, the existence of MnO$_2$ improved the specific capacity, which may have been due to the synergistic effect of MnO$_2$ and rGO. The initial specific capacities of Si@MnO$_2$@rGO-20°C and Si@MnO$_2$@rGO-160°C were 1670.24 and 2450.32 mAh g^{-1}, respectively. Furthermore, after 100 cycles, the specific capacities were 512.14 and 665.19 mAh g^{-1}, respectively, with low capacity retention rates. The initial specific capacity of Si@MnO$_2$@rGO-50°C was 1378.14 mAh g^{-1}; after 150 cycles, the capacity was maintained at 960.21 mAh g^{-1}. Among Si@MnO$_2$@rGO-50°C, Si@MnO$_2$@rGO-20°C, and Si@MnO$_2$@rGO-160°C, although the Si@MnO$_2$@rGO-50°C exhibited a lower capacity, it had the excellent cyclability, which can better meet the commercial need of long lifetime, due to the stability of the sea urchin-like Si@MnO$_2$@rGO-50°C and the dual protection of rGO and MnO$_2$. Interestingly, the structure of rGO encapsulating the sea urchin-like Si@MnO$_2$-50°C mitigated the volume-change effects of Si nanospheres, improving the electrical conductivity and contributing to the high capacity when comparing the Si and Si@MnO$_2$-50°C. A comparison of the rate and cycling performances of the sea urchin-like Si@MnO$_2$@rGO-50°C, at different various current densities, is shown in Figure 5d. At current densities of 0.1, 0.2, 0.5, 1, and 2 A g^{-1}, the specific charging capacities were 1323.87, 971.85, 701.12, 491.85, and 272.47 mAh g^{-1}, respectively. Furthermore, when the current density rose again to 0.1 A g^{-1}, the specific charging capacity recovered to 981.68 mAh g^{-1} and the capacity retention rate was 74.2%. Compared to previous reports of Si and Si@rGO, Si@MnO$_2$@rGO-50°C demonstrated a long lifetime and high capacity retention rates [46,47]. Furthermore, to evaluate the cycling stability at high current densities, Si@MnO$_2$@rGO-50°C was tested at 1 Ah g^{-1} (Figure 5e). In the first charge/discharge cycle, the specific capacity was 1446.85 mAh g^{-1}; after 1000 cycles, the specific capacity was 1282.72 mAh g^{-1} with a coulombic efficiency of 99.4%. The composite material also showed excellent cycling performance at high currents. The decrease in capacity fluctua-

tions at the first 80 cycles was due to the irreversible formation of SEI film on the materials' surface. Interestingly, the capacity exhibited an increasing trend from the ~80th cycle upwards. This was attributed to the reversible growth of a polymeric gel-like film. After a long-cycling charging/discharging process, the polymeric gel-like film gradually degraded. The improved electrode kinetics increased the capacity. This phenomenon has been widely reported among transition metal oxides [48–55]. Table S2 shows the performance comparison among the reported works and indicates the high capacity and long lifetime of Si@MnO$_2$@rGO-50°C. When the cycle reached 150 times, the specific capacity was 960.21 mAh g^{-1} at 0.1 A g^{-1} and 746.13 mA g^{-1} at 1 A g^{-1}. This is because the higher the charge/discharge current density was, the fast the electrode chemical reaction speed became. A large number of lithium ions reacted on the surface of the anode materials instantly, leading to the formation of concentration polarization on the electrode surface. Part of the active materials had no time to react, and the utilization rate of the active materials became smaller, resulting in the decreasing in capacity.

EIS measurements were carried out to further investigate the electrochemical mechanism shown in Figure 6. Figure 6a shows the EIS plots and corresponding fitting plots of Si, Si@MnO$_2$-50°C, and Si@MnO$_2$@rGO-50°C, respectively. Additionally, the inset shows the data equivalent circuit diagrams. The EIS diagram consists of a semicircle in the mid-high-frequency region and a diagonal line in the low-frequency region. Here, R$_{CT}$ in the mid-frequency region corresponds to the charge-transfer impedance and W$_O$ in the low-frequency region corresponds to the diffusion of Li$^+$ inside the electrode material [56,57]. The R$_S$ and R$_{CT}$ values fitted from the equivalent circuit model are summarized in Table S3 for comparison. The Si@MnO$_2$@rGO-50°C exhibited a low value of R$_{CT}$ (146.2 Ω) before cycling, which was the lowest among Si, Si@MnO$_2$@rGO-50°C, and Si@MnO$_2$-50°C. This result was attributed to the rGO networks, prominently improving the electronic conductivity of the electrodes and lowering the charge transfer impedance. Figure 6b shows the EIS plots and corresponding fitting plots of Si@MnO$_2$@rGO-50°C before and after 150 cycles at 0.1 A g^{-1}; cycled Si@MnO$_2$@rGO-50°C was fitted with the same equivalent circuit model in Figure 6a. The R$_{CT}$ (72.7 Ω) was lower after cycling, which implies the charge transfer impedance decreased substantially, demonstrating the stable SEI film and good structure stability during cycling of Si@MnO$_2$@rGO-50°C.
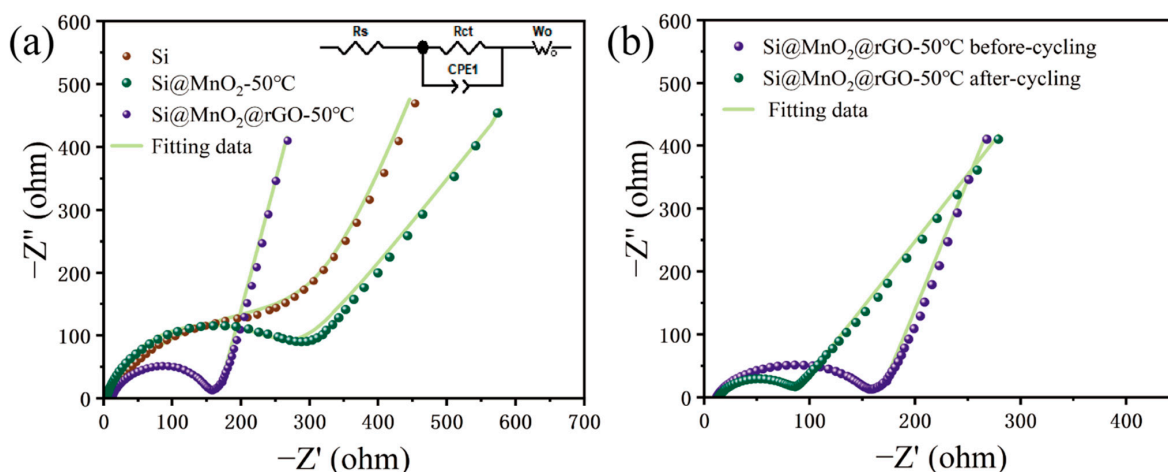
Figure 6. (**a**) The electrochemical impedance spectra of Si, Si@MnO$_2$-50°C, and Si@MnO$_2$@rGO-50°C. The inset shows the equivalent circuit model. (**b**) The electrochemical impedance spectra of the Si@MnO$_2$@rGO-50°C before and after cycling.

Figure 7a,b shows the cross-sectional SEM images of Si before and after 150 cycles at 0.1 A g^{-1}. After cycles, the volume expansion was ~323% (from 5.3 μm to 22.41 μm). The huge change in volume expansion of Si may have contributed to the intercalation and deintercalation of lithium ions during cycles and the exfoliation of the active materials. As

shown in Figure S1a,b, the volume expansion of Si@MnO$_2$-50°C electrode after 150 cycles at 0.1 A g^{-1} was ~198% (from 4.29 μm to 12.8 μm). Interestingly, the volume expansion of Si@MnO$_2$@rGO-50°C electrode was ~59% (8.13 μm to 12.9 μm) after 150 cycles at 0.1 A g^{-1}. Such a small volume change in the active materials guarantees long-term cycling stability. Figure S2a shows the top-view SEM image of Si@MnO$_2$@rGO-50°C after 150 cycles at 0.1 A g^{-1}. The electrode sheet was relatively intact without signs of rupture. Figure S2b shows the element mapping of Figure S2a, suggesting Si, Mn, O, and C were evenly distributed. The mechanism of the Si electrode reaction was further illustrated in Figure 7e. The lithiation of Si resulted in the formation of an amorphous silicon–lithium alloy (Li$_x$Si) (0.16 V). Then, the amorphous Li$_x$Si was transformed to crystalline Li$_{15}$Si$_4$ (0.1 V). The delithiation process involved the transformation from crystalline Li$_{15}$Si$_4$ to amorphous Li$_x$Si (0.24 V) and, finally, to amorphous Si (0.5 V) [58–60].
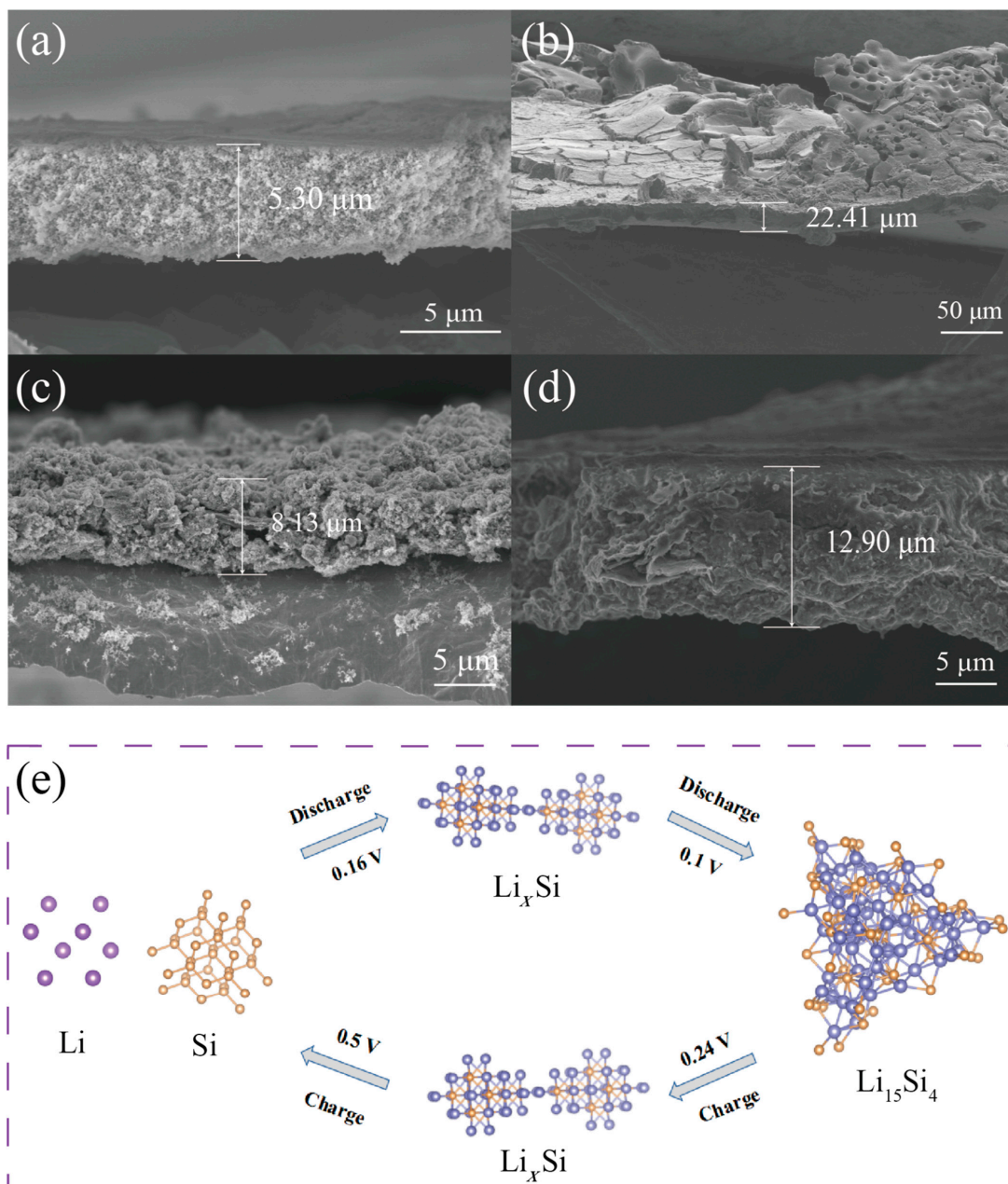

Figure 7. (**a,b**) Cross-sectional SEM images of Si before and after 150 cycles. (**c,d**) Cross-sectional SEM images of Si@MnO$_2$@rGO-50°C before and after 150 cycles. (**e**) The mechanism of intercalation and deintercalation of lithium ions.

4. Conclusions

In summary, sea urchin-like $Si@MnO_2@rGO-50°C$ as an anode for lithium-ion batteries was presented. The reversible capacity, cyclability, and rate capability were very high, which was attributed to the dual protection of rGO and MnO_2. The discharge specific capacity was maintained at 1282.72 mAh g^{-1} under a test current of 1 A g^{-1} after more than 1000 cycles. Such high cyclability may be attributed to the sea urchin-like structure reducing the volume expansion of anodes during the charging/discharging process. The present results indicate that the sea urchin-like $Si@MnO_2@rGO-50°C$ is a good candidate for high performance anodes of lithium-ion batteries. This work made efforts to develop efficient methods to store clean energy and achieve carbon neutrality.

Supplementary Materials: The following supporting information can be downloaded at: https://www.mdpi.com/article/10.3390/nano12020285/s1. Figure S1: (a,b) Cross-sectional SEM images of $Si@MnO_2-50°C$ before and after 150 cycles. Figure S2: (a) Cross-sectional SEM images of the $Si@MnO_2@rGO-50°C$ electrode sheet after 150 cycles at 0.1 A g^{-1}. (b) Element mapping images of the $Si@MnO_2@rGO-50°C$ electrode sheet after 150 cycles at 0.1 A g^{-1}. Table S1: Capacity contribution of Si, MnO_2, and rGO. Table S2: Synthesis strategies and electrochemical performance comparison of Si-based anode materials and MnO_2-based anode materials in lithium-ion batteries (References [61–64] are cited in Table S2). Table S3: The R_S and R_{CT} values fitted from the equivalent circuit model are summarized for comparison.

Author Contributions: Conceptualization, J.L. and M.W.; methodology, Q.W.; software, X.Z.; validation, Y.S. and T.Z.; formal analysis, J.L.; investigation, J.L.; resources, J.L.; data curation, J.L.; writing—original draft preparation, J.L.; writing—review and editing, J.L.; visualization, J.S.; supervision, J.S.; project administration, J.S.; funding acquisition, J.S. All authors have read and agreed to the published version of the manuscript.

Data Availability Statement: The data presented in this study are available on request from the corresponding author.

Conflicts of Interest: The authors declare no conflict of interest.

References

1. Mo, R.W.; Li, F.; Tan, X.Y.; Xu, P.C.; Tao, R.; Shen, G.R.; Lu, X.; Liu, F.; Shen, L.; Xu, B.; et al. High-quality mesoporous graphene particles as high-energy and fast-charging anodes for lithium-ion batteries. *Nat. Commun.* **2019**, *10*, 1474. [CrossRef]
2. Grey, P.; Hall, D.S. Prospects for lithium-ion batteries and beyond-a 2030 vision. *Nat. Commun.* **2020**, *11*, 6279. [CrossRef] [PubMed]
3. Yang, Y.; McDowell, M.T.; Jackson, A.; Cha, J.J.; Hong, S.S.; Cui, Y. New Nanostructured Li_2S/Silicon Rechargeable Battery with High Specific Energy. *Nano Lett.* **2010**, *10*, 1486–1491. [CrossRef] [PubMed]
4. Ge, F.; Li, G.C.; Wang, X.C.; Chen, X.X.; Fu, L.; Liu, X.X.; Mao, E.Y.; Liu, J.; Yang, X.L.; Qian, C.X.; et al. Manipulating Oxidation of Silicon with Fresh Surface Enabling Stable Battery Anode. *Nano Lett.* **2021**, *21*, 3127–3133. [CrossRef] [PubMed]
5. Zheng, G.R.; Xiang, Y.X.; Xu, L.F.; Luo, H.; Wang, B.L.; Liu, Y. Controlling Surface Oxides in Si/C Nanocomposite Anodes for High-Performance Li-Ion Batteries. *Adv. Energy Mater.* **2018**, *8*, 1801718. [CrossRef]
6. Zheng, T.Y.; Jia, Z.; Lin, N.; Langer, T.; Lux, S.; Lund, I.; Gentschev, A.C.; Qiao, J.; Liu, G. Molecular Spring Enabled High-Performance Anode for Lithium Ion Batteries. *Polymers* **2017**, *9*, 657. [CrossRef] [PubMed]
7. Yue, H.W.; Li, Q.; Liu, D.Q.; Hou, X.Y.; Bai, S.; Lin, S.M.; He, D.Y. High-yield fabrication of graphene-wrapped silicon nanoparticles for self-support and binder-free anodes of lithium-ion batteries. *J. Alloy. Compd.* **2018**, *744*, 243–251. [CrossRef]
8. Gao, R.S.; Tang, J.; Tang, S.; Zhang, K.; Ozawa, K.; Qin, L.C. Biomineralization-inspired: Rapid preparation of a silicon-based composite as a high-performance lithium-ion battery anode. *J. Mater. Chem. A* **2021**, *9*, 11614–11622. [CrossRef]
9. Fang, R.; Miao, C.; Mou, H.Y.; Xiao, W. Facile synthesis of $Si@TiO_2@rGO$ composite with sandwich-like nanostructure as superior performance anodes for lithium ion batteries. *J. Alloy. Compd.* **2020**, *818*, 152884. [CrossRef]
10. Hassan, F.; Batmaz, R.; Li, J.D.; Wang, X.L.; Xiao, X.C.; Yu, A.P.; Chen, Z.W. Evidence of covalent synergy in silicon–sulfur–graphene yielding highly efficient and long-life lithium-ion batteries. *Nat. Commun.* **2015**, *26*, 8597. [CrossRef] [PubMed]

11. Wang, Z.L.; Mao, Z.M.; Lai, L.F.; Okubo, M.; Song, Y.H.; Zhou, Y.J.; Liu, X.; Huang, W. Sub-micron silicon/pyrolyzed carbon@natural graphite self-assembly composite anode material for lithium-ion batteries. *Chem. Eng. J.* **2017**, *313*, 187–196. [CrossRef]

12. Dai, J.Y.; Liao, J.; He, M.Y.; Yang, M.M.; Wu, K.P.; Yao, W.T. Si@SnS$_2$-rGO composite anode material with high lithium-ion battery capacity. *ChemSusChem* **2019**, *12*, 5092–5098. [CrossRef] [PubMed]

13. Yang, Z.; Song, Y.W.; Zhang, C.F.; He, J.J.; Li, X.D.; Wang, X.; Wang, N.; Li, Y.L.; Huang, C.S. Porous 3D Silicon-Diamondyne Blooms Excellent Storage and Diffusion Properties for Li, Na, and K Ions. *Adv. Energy Mater.* **2021**, *11*, 2101197. [CrossRef]

14. Wu, Y.J.; Chen, Y.A.; Huang, C.L.; Su, J.T.; Hsieh, C.T.; Lu, S.Y. Small highly mesoporous silicon nanoparticles for high performance lithium ion based energy storage. *Chem. Eng. J.* **2020**, *400*, 125958. [CrossRef]

15. Liang, B.R.; Zhu, S.S.; Wang, J.C.; Liang, X.Q.; Huang, H.F.; Huang, D.; Zhou, W.Z.; Xu, S.K.; Guo, J. Silicon-doped FeOOH nanorods@graphene sheets as high-capacity and durable anodes for lithium-ion batteries. *Appl. Surf. Sci.* **2021**, *550*, 149330. [CrossRef]

16. Zhang, Y.L.; Mu, Z.J.; Lai, J.P.; Chao, Y.G.; Yang, Y.; Zhou, P.; Li, Y.J.; Yang, W.X.; Xia, Z.H.; Guo, S.J. MXene/Si@SiO$_X$@C Layer-by-Layer Superstructure with Auto-Adjustable Function for Superior Stable Lithium Storage. *ACS Nano* **2019**, *13*, 2167–2175. [PubMed]

17. Suo, G.Q.; Zhang, J.Q.; Li, D.; Yu, Q.Y.; Wang, W.A.; He, M.; Feng, L.; Hou, X.J.; Yang, Y.L.; Ye, X.H.; et al. N-doped carbon/ultrathin 2D metallic cobalt selenide core/sheath flexible framework bridged by chemical bonds for high-performance potassium storage. *Chem. Eng. J.* **2020**, *388*, 124396. [CrossRef]

18. Kang, Y.; Zhang, Y.H.; Shi, Q.; Shi, H.W.; Xue, D.F.; Shi, F.N. Highly efficient Co$_3$O$_4$/CeO$_2$ heterostructure as anode for lithium-ion batteries. *J. Colloid Interf. Sci.* **2020**, *585*, 705–715. [CrossRef]

19. Li, D.P.; Dai, L.N.; Ren, X.H.; Ji, F.J.; Sun, Q.; Zhang, Y.M.; Ci, L.J. Foldable Potassium-Ion Batteries Enabled by Free-standing and Flexible SnS$_2$@C Nanofibers. *Energy Environ. Sci.* **2021**, *14*, 424–436. [CrossRef]

20. Pham, T.K.; Shin, J.H.; Karima, N.C.; Jun, Y.S.; Jeong, S.K.; Cho, N.; Lim, S.N. Application of recycled Si from industrial waste towards Si/rGO composite material for long lifetime lithium-ion battery. *J. Power Sources* **2021**, *506*, 230244. [CrossRef]

21. Chen, X.F.; Yang, X.F.; Pan, F.L.; Zhang, T.T.; Zhu, X.Y.; Qiu, J.Y.; Li, M.; Mu, Y.; Ming, H. Fluorine-functionalized core-shell Si@C anode for a high-energy lithium-ion full battery. *J. Alloy. Compd.* **2021**, *884*, 160945. [CrossRef]

22. Tu, W.M.; Bai, Z.Y.; Deng, Z.; Zhang, H.N.; Tang, H.L. In-Situ Synthesized Si@C Materials for the Lithium Ion Battery: A Mini Review. *Nanomaterials* **2019**, *9*, 432. [CrossRef]

23. Gou, W.W.; Kong, X.Z.; Wang, Y.P.; Ai, Y.L.; Liang, S.Q.; Pan, A.Q.; Cao, G.Z. Yolk-shell structured V$_2$O$_3$ microspheres wrapped in N, S co-doped carbon as Pea-Pod nanofibers for high-capacity lithium ion batteries. *Chem. Eng. J.* **2019**, *374*, 545–553. [CrossRef]

24. Wu, F.F.; Gao, X.B.; Xu, X.L.; Jiang, Y.N.; Gao, X.L.; Yin, R.L.; Shi, W.H.; Liu, W.X.; Lu, G.; Cao, X.H. MnO$_2$ nanosheet-assembled hollow polyhedron grown on carbon cloth for flexible aqueous zinc-ion batteries. *ChemSusChem* **2020**, *13*, 1537–1545. [CrossRef] [PubMed]

25. Zhao, Y.; He, J.F.; Dai, M.Z.; Zhao, D.P.; Wu, X.; Liu, B.D. Emerging CoMn-LDH@MnO$_2$ electrode materials assembled using nanosheets for flexible and foldable energy storage devices. *J. Energy Chem.* **2020**, *45*, 67–73. [CrossRef]

26. Zhang, Y.; Ren, J.H.; Xu, T.; Feng, A.L.; Hu, K.; Yu, N.F.; Xia, Y.B.; Zhu, Y.S.; Huang, Z.Y.; Wu, G.L. Covalent Bonding of Si Nanoparticles on Graphite Nanosheets as Anodes for Lithium-Ion Batteries Using Diazonium Chemistry. *Nanomaterials* **2019**, *9*, 1741. [CrossRef] [PubMed]

27. Liu, F.S.; Xiao, Y.Y.; Liu, Y.T.; Han, P.Y.; Qin, G.H. Mesoporous MnO$_2$ based composite electrode for efficient alkali-metal-ion storage. *Chem. Eng. J.* **2020**, *380*, 122487. [CrossRef]

28. Wang, B.Y.; Wei, Y.H.; Fang, H.Y.; Qiu, X.L.; Zhang, Q.B.; Wu, H.; Wang, Q.; Zhang, Y.; Ji, X.B. Mn-substituted tunnel-type polyantimonic acid confined in a multidimensional integrated architecture enabling superfast-charging lithium-ion battery anodes. *Adv. Sci.* **2021**, *8*, 2002866. [CrossRef]

29. Pi, W.B.; Mei, T.; Li, J.; Wang, J.Y.; Li, J.H.; Wang, X.B. Durian-like NiS$_2$@rGO nanocomposites and their enhanced rate performance. *Chem. Eng. J.* **2018**, *335*, 275–281. [CrossRef]

30. Mei, L.; Xu, C.; Yang, T.; Ma, J.M.; Chen, L.B.; Li, Q.H.; Wang, T.H. Superior electrochemical performance of ultrasmall SnS$_2$ nanocrystals decorated on flexible RGO in lithium-ion batteries. *J. Mater. Chem. A* **2013**, *1*, 8658–8664. [CrossRef]

31. Rana, M.; He, Q.; Luo, B.; Lin, T.; Ran, L.B.; Li, M.; Gentle, I.; Knibbe, R. Multifunctional Effects of Sulfonyl-Anchored, Dual-Doped Multilayered Graphene for High Areal Capacity Lithium Sulfur Batteries. *ACS Cent. Sci.* **2019**, *5*, 1946–1958. [CrossRef]

32. Park, S.; Jeong, S.Y.; Lee, T.K.; Park, M.W.; Lim, H.Y.; Sung, J.; Cho, J.; Kwak, S.K.; Hong, S.Y.; Choi, N.S. Replacing conventional battery electrolyte additives with dioxolone derivatives for high-energy-density lithium-ion batteries. *Nat. Commun.* **2021**, *12*, 838. [CrossRef] [PubMed]

33. Cui, R.Y.; Hultman, N.; Cui, D.; McJeon, H.; Yu, S.; Edwards, M.R.; Sen, A.; Song, K.; Bowman, C.; Clarke, L.; et al. A plant-by-plant strategy for high-ambition coal power phaseout in China. *Nat. Commun.* **2021**, *12*, 1468. [CrossRef]

34. Zhao, T.M.; Zheng, C.W.; He, H.X.; Guan, H.Y.; Zhong, T.Y.; Xing, L.L.; Xue, X.Y. A self-powered biosensing electronic-skin for real-time sweat Ca^{2+} detection and wireless data transmission. *Smart Mater. Struct.* **2019**, *28*, 085015. [CrossRef]

35. Chen, S.; Chen, Z.; Xu, X.Y.; Cao, C.B.; Xia, M.; Luo, Y.J. Scalable 2D Mesoporous Silicon Nanosheets for High-Performance Lithium-Ion Battery Anode. *Small* **2018**, *14*, 1703361. [CrossRef] [PubMed]

36. Zhao, T.M.; Han, Y.C.; Qin, L.N.; Guan, H.Y.; Xing, L.L.; Li, X.J.; Xue, X.Y.; Li, G.L.; Zhan, Y. Bidirectional modulation of neural plasticity by self-powered neural stimulation. *Nano Energy* **2021**, *85*, 106006. [CrossRef]

37. Liu, H.D.; Hu, Z.L.; Su, Y.Y.; Ruan, H.B.; Hu, R.; Zhang, L. MnO_2 nanorods/3D-rGO composite as high performance anode materials for Li-ion batterie. *Appl. Surf. Sci.* **2017**, *392*, 777–784. [CrossRef]

38. Li, Y.; Ye, D.X.; Liu, W.; Shi, B.; Guo, R.; Pei, H.J.; Xie, J.Y. A three-dimensional core-shell nanostructured composite of polypyrrole wrapped MnO_2/reduced graphene oxide/carbon nanotube for high performance lithium ion batteries. *J. Colloid Interf. Sci.* **2017**, *493*, 241–248. [CrossRef]

39. Xu, P.; Chen, H.Y.; Zhou, X.; Xiang, H.F. Gel polymer electrolyte based on PVDF-HFP matrix composited with rGO-PEG-NH_2 for high-performance lithium ion battery. *J. Membr. Sci.* **2021**, *617*, 118660. [CrossRef]

40. Li, J.B.; Ding, Z.B.; Li, J.L.; Wang, C.Y.; Pan, L.K.; Wang, G.X. Synergistic coupling of $NiS_{1.03}$ nanoparticle with S-doped reduced graphene oxide for enhanced lithium and sodium storage. *Chem. Eng. J.* **2020**, *407*, 127199. [CrossRef]

41. Fang, Y.Z.; Hu, R.; Liu, B.Y.; Zhang, Y.Y.; Zhu, K.; Yan, J.; Ye, K.; Cheng, K.; Wang, G.L.; Cao, D.X. MXene-derived TiO_2/reduced graphene oxide composite with an enhanced capacitive capacity for Li-ion and K-ion batteries. *J. Mater. Chem. A* **2019**, *7*, 5363–5372. [CrossRef]

42. Yao, W.Q.; Wu, S.B.; Zhan, L.; Wang, Y.L. Two-dimensional Porous Carbon-coated Sandwich-like Mesoporous SnO_2/Graphene/ Mesoporous SnO_2 Nanosheets towards High-Rate and Long Cycle Life Lithium-ion Batteries. *Chem. Eng. J.* **2018**, *361*, 329–341. [CrossRef]

43. Chae, S.; Choi, S.H.; Kim, N.; Sung, J.; Cho, J. Integration of Graphite and Silicon Anodes for the Commercialization of High-Energy Lithium-Ion Batteries. *Angew. Chem. Int. Ed.* **2019**, *59*, 110–135. [CrossRef] [PubMed]

44. Li, Z.H.; Zhang, Y.P.; Liu, T.F.; Gao, X.H.; Li, S.Y.; Ling, M.; Liang, C.D.; Zheng, J.C.; Lin, Z. Silicon Anode with High Initial Coulombic Efficiency by Modulated Trifunctional Binder for High-Areal-Capacity Lithium-Ion Batteries. *Adv. Energy Mater.* **2020**, *10*, 1903110. [CrossRef]

45. Keller, C.; Desrues, A.; Karuppiah, S.; Martin, E.; Alper, J.; Boismain, F.; Villevieille, C.; Herlin-Boime, N.; Haon, C.; Chenevier, P. Effect of Size and Shape on Electrochemical Performance of Nano-Silicon-Based Lithium Battery. *Nanomaterials* **2021**, *11*, 307. [CrossRef]

46. Zhao, Z.Q.; Cai, X.; Yu, X.Y.; Wang, H.Q.; Li, Q.Y.; Fang, Y.P. Zinc-assisted Mechanochemical Coating of Reduced Graphene Oxide Thin Layer on Silicon Microparticles for Efficient Lithium-ion Battery Anodes. *Sustain. Energy Fuels.* **2019**, *3*, 1258–1268. [CrossRef]

47. Li, X.; Bai, Y.S.; Wang, M.S.; Wang, G.L.; Ma, Y.; Huang, Y.; Zheng, J.M. Dual Carbonaceous Materials Synergetic Protection Silicon as a High-Performance Free-Standing Anode for Lithium-Ion Battery. *Nanomaterials* **2019**, *9*, 650. [CrossRef] [PubMed]

48. Laruelle, S.; Grugeon, S.; Poizot, P.; Dolle, M.; Dupont, L.; Tarascon, J.M. On the Origin of the Extra Electrochemical Capacity Displayed by MO/Li Cells at Low Potential. *J. Electrochem. Soc.* **2002**, *149*, A627–A634. [CrossRef]

49. Hao, Q.; Wang, J.P.; Xu, C.X. Facile preparation of Mn_3O_4 octahedra and their long-term cycle life as an anode material for Li-ion batteries. *J. Mater. Chem. A* **2014**, *2*, 87–93. [CrossRef]

50. Li, L.; Guo, Z.P.; Du, A.J.; Liu, H.K. Rapid microwave-assisted synthesis of Mn_3O_4-graphene nanocomposite and its lithium storage properties. *J. Mater. Chem.* **2012**, *22*, 3600–3605. [CrossRef]

51. Jiang, Y.; Jiang, Z.J.; Chen, B.H.; Jiang, Z.Q.; Cheng, S.; Rong, H.B.; Huang, J.L.; Liu, M.L. Morphology and crystal phase evolution induced performance enhancement of MnO_2 grown on reduced graphene oxide for lithium ion batteries. *J. Mater. Chem. A* **2016**, *4*, 2643–2650. [CrossRef]

52. Kim, K.; Daniel, G.; Kessler, V.G.; Seisenbaeva, G.A.; Pol, V.G. Basic Medium Heterogeneous Solution Synthesis of alpha-MnO_2 Nanoflakes as an Anode or Cathode in Half Cell Configuration (vs. Lithium) of Li-Ion Batteries. *Nanomaterials* **2018**, *8*, 608. [CrossRef]

53. Liu, C.; Wu, X.; Wang, B. Performance modulation of energy storage devices: A case of Ni-Co-S electrode materials. *Chem. Eng. J.* **2020**, *392*, 123651. [CrossRef]

54. Wu, X.; Yao, S.Y. Flexible electrode materials based on WO_3 nanotube bundles for high performance energy storage devices. *Nano Energy* **2017**, *42*, 143–150. [CrossRef]

55. Zhang, D.A.; Wang, Q.; Wang, Q.; Sun, J.; Xing, L.L.; Xue, X.Y. High capacity and cyclability of hierarchical MoS_2/SnO_2 nanocomposites as the cathode of lithium-sulfur battery. *Electrochim. Acta.* **2015**, *173*, 472–482. [CrossRef]

56. Chen, Y.X.; Yan, Y.J.; Liu, X.L.; Zhao, Y.; Wu, X.Y.; Zhou, J.; Wang, Z.F. Porous Si/Fe_2O_3 Dual Network Anode for Lithium–Ion Battery Application. *Nanomaterials* **2020**, *10*, 2331. [CrossRef]

57. Zhang, Y.; Hu, K.; Zhou, Y.L.; Xia, Y.B.; Yu, N.F.; Wu, G.L.; Zhu, Y.S.; Wu, Y.P.; Huang, H.B. A Facile, One-Step Synthesis of Silicon/Silicon Carbide/Carbon Nanotube Nanocomposite as a Cycling-Stable Anode for Lithium Ion Batteries. *Nanomaterials* **2019**, *9*, 1624. [CrossRef] [PubMed]

58. Han, N.; Li, J.J.; Wang, X.C.; Zhang, C.L.; Liu, G.; Li, X.H.; Qu, J.; Peng, Z.; Zhu, X.Y.; Zhang, L. Flexible Carbon Nanotubes Confined Yolk-Shelled Silicon-Based Anode with Superior Conductivity for Lithium Storage. *Nanomaterials* **2021**, *11*, 699. [CrossRef] [PubMed]

59. Kwon, H.J.; Hwang, J.Y.; Shin, H.J.; Jeong, M.G.; Chung, K.Y.; Sun, Y.K.; Jung, H.G. Nano/Microstructured Silicon–Carbon Hybrid Composite Particles Fabricated with Corn Starch Biowaste as Anode Materials for Li-Ion Batteries. *Nano Lett.* **2019**, *20*, 625–635. [CrossRef] [PubMed]

60. Argyropoulos, D.P.; Zardalidis, G.; Giotakos, P.; Daletou, M.; Farmakis, F. Study of the Role of Void and Residual Silicon Dioxide on the Electrochemical Performance of Silicon Nanoparticles Encapsulated by Graphene. *Nano Lett.* **2021**, *11*, 2864. [CrossRef] [PubMed]

61. Gao, X.F.; Li, J.Y.; Xie, Y.Y.; Guan, D.S.; Yuan, C. A Multilayered Silicon-Reduced Graphene Oxide Electrode for High Performance Lithium-Ion Batteries. *ACS Appl. Mater. Interfaces.* **2015**, *7*, 7855–7862. [CrossRef] [PubMed]

62. Wang, T.H.; Ji, X.; Wu, F.Z.; Yang, W.L.; Dai, X.Y.; Xu, X.J.; Wang, J.; Guo, D.; Chen, M.L. Facile fabrication of a three-dimensional coral-like silicon nanostructure coated with a C/rGO double layer by using the magnesiothermic reduction of silica nanotubes for high-performance lithium-ion battery anodes. *J. Alloys Compd.* **2021**, *863*, 158569. [CrossRef]

63. Wang, D.X.; Wang, Y.; Li, Q.Y.; Guo, W.B.; Zhang, F.C.; Niu, S.S. Urchin-like alpha-Fe_2O_3/MnO_2 hierarchical hollow composite microspheres as lithium-ion battery anodes. *J. Power Sources.* **2018**, *393*, 186–192. [CrossRef]

64. Ma, Z.F.; Zhao, T.B. Reduced graphene oxide anchored with MnO_2 nanorods as anode for high rate and long cycle Lithium ion batteries. *Electrochim. Acta.* **2016**, *201*, 165–171. [CrossRef]